

CELL BIOLOGY

KIF13A motors are regulated by Rab22A to function as weak dimers inside the cell

Nishaben M. Patel¹, Meenakshi Sundaram Aravintha Siva¹, Ruchi Kumari¹, Dipeshwari J. Shewale¹, Ashim Rai², Michael Ritt², Prerna Sharma³, Subba Rao Gangi Setty³, Sivaraj Sivaramakrishnan², Virupakshi Soppina^{1*}

Endocytic recycling is a complex itinerary, critical for many cellular processes. Membrane tubulation is a hallmark of recycling endosomes (REs), mediated by KIF13A, a kinesin-3 family motor. Understanding the regulatory mechanism of KIF13A in RE tubulation and cargo recycling is of fundamental importance but is overlooked. Here, we report a unique mechanism of KIF13A dimerization modulated by Rab22A, a small guanosine triphosphatase, during RE tubulation. A conserved proline between neck coil-coiled-coil (NC-CC1) domains of KIF13A creates steric hindrance, rendering the motors as inactive monomers. Rab22A plays an unusual role by binding to NC-CC1 domains of KIF13A, relieving proline-mediated inhibition and facilitating motor dimerization. As a result, KIF13A motors produce balanced motility and force against multiple dyneins in a molecular tug-of-war to regulate RE tubulation and homeostasis. Together, our findings demonstrate that KIF13A motors are tuned at a single-molecule level to function as weak dimers on the cellular cargo.

INTRODUCTION

Recycling endocytosis is essential for trafficking internalized cargoes, such as membrane receptors and neurotransmitters, back to the cell periphery to maintain plasma membrane composition and cellular homeostasis (1). Recycling endosomes (REs) play an important role in multiple cellular processes such as cytokinesis, secretion, and adhesion (2). Malfunction in recycling has been implicated in multiple developmental disorders, Alzheimer's disease, Huntington's disease, microvillus inclusion disease (MVID), aging, and cancer (1, 3, 4). REs are characterized by highly pleomorphic and dynamic tubular and vesicular structures. Rab guanosine triphosphatases (GTPases) are the membrane organizers that play vital roles in endosomal function by their ability to recruit molecular motors to respective sorting vesicles. Several members of Rab GTPases (such as Rab8A, Rab10, Rab11A, Rab22A, and Rab35A) are implicated in the regulation of RE tubulation and cargo recycling (5–12), yet the underlying molecular mechanism of Rab-mediated RE tubulation is poorly understood.

Endocytosis heavily relies on activity of microtubule (MT)-based molecular motors, kinesins, and dyneins, which play various roles within cells, including intracellular cargo transport (13–16). Kinesins are generally composed of an N-terminal globular catalytic head called motor domain (MD), a short neck linker that connects MD to the stalk, a dimerization domain called neck coil (NC), multiple coiled-coil (CC) domains, and a C-terminal cargo-binding tail domain (Fig. 1A). Hydrolysis of adenosine 5'-triphosphate (ATP) to generate force (~6 pN) and ability of the NC domain to dimerize MD are the key attributes of kinesin motors involved in cargo transport (17). A kinesin monomer fails to move processively, the ability to take several steps without disengaging from the MT, a property essential for cargo transport. The NC domain allows dimerization

of kinesin motor, and coupling of this with ATP hydrolysis in MD enables kinesin dimers to take multiple steps and generate sufficient force (~6 pN), effectively transporting cargo along MTs (15, 18, 19). Dynein is a multisubunit complex responsible for the majority of retrograde cargo trafficking (20). In comparison to kinesin, dynein exerts lesser force (~1 pN) but work collectively as a team on the cargo to generate large forces necessary for multiple cellular functions (16, 21, 22). Abnormalities in kinesin or dynein assembly and function have been implicated in developmental defects, neurodegeneration, and cancer (23–25).

KIF13A, a member of kinesin-3 family, plays an indispensable role in generation of RE tubules by interacting with multiple Rabs (6, 26). Our previous *in vitro* single-molecule studies demonstrated that proline at the junction of NC and CC1, domains responsible for motor dimerization, renders wild-type (WT) KIF13A motor as an inactive monomer and does not allow MT-based motility (15). Proline creates steric hindrance, when present in the α helix core and breaks the helix (27–30), as observed in KIF13A (15, 31, 32). Deletion of this proline (Δ P390) relieves this hindrance and results in a constitutively active KIF13A dimer (hereafter referred to as Δ P) through intermolecular NC-CC1 interaction and displays robust MT-based superprocessive motility (15). Although WT KIF13A is inactive *in vitro*, it plays an essential role in recycling endocytosis. How a KIF13A WT motor containing proline overcomes this inhibition and generates cytoplasmic RE tubules in cells is enigmatic and of fundamental interest.

In the present study, we propose and demonstrate the *in vivo* mechanism that KIF13A uses to overcome proline-induced inhibition and efficiently pull membranous tubular REs in the cytoplasm. We observed that tubular REs are formed as a result of molecular tug-of-war between kinesin (KIF13A) and dynein. Our findings demonstrate that Rab22A is a key modulator for regulation of KIF13A dimerization, motility, and force generation, essential for RE tubulation and cargo recycling. We show that direct binding of Rab22A to NC-CC1 domains relieves proline-induced kink and favors intermolecular NC-CC1 interaction. This results in processive KIF13A dimer, critical for RE tubulation and endocytic cargo recycling.

¹Biological Engineering, Indian Institute of Technology Gandhinagar, Gandhinagar, India. ²Department of Genetics, Cell Biology, and Development, University of Minnesota, Minneapolis, MN, USA. ³Department of Microbiology and Cell Biology, Indian Institute of Science, Bangalore, India.

*Corresponding author. Email: vsoppina@gmail.com, vsoppina@iitgn.ac.in

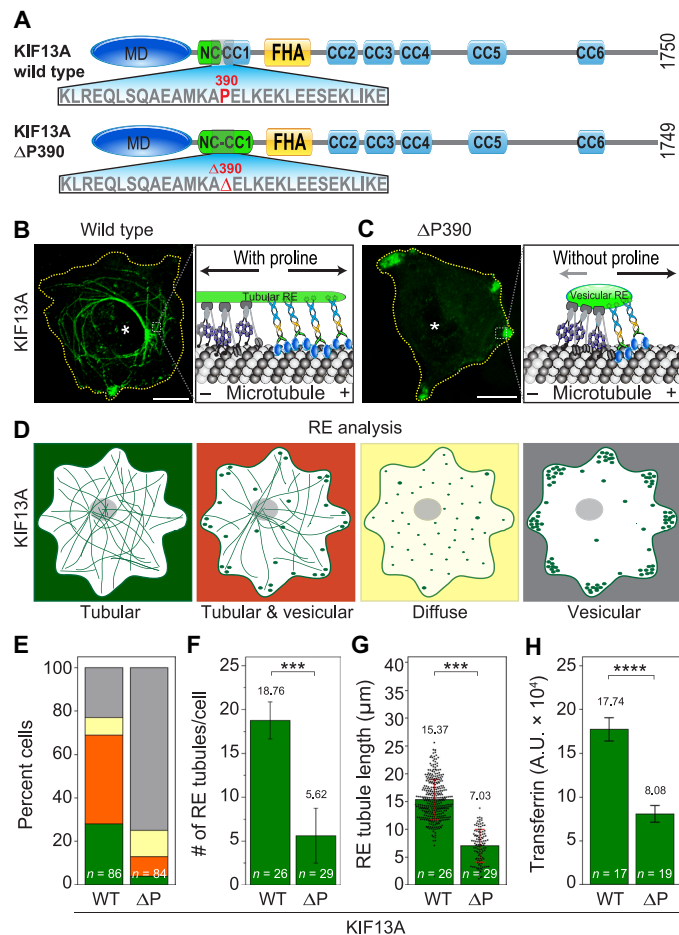


Fig. 1. KIF13A WT and ΔP motors display discrete RE morphology. (A) Domain organization of full-length KIF13A WT and ΔP motors. (B and C) HeLa cells expressing KIF13A WT (B) and ΔP390 motors (C) and schematic representation of RE morphology and distribution are depicted in respective panels to their right. (D and E) Cartoon diagram (D) depicting categories for the quantification of RE tubulation and (E) percentage of transfected cells with tubular REs, both tubular and vesicular REs, and diffuse (no REs) and vesicular REs. Data presented from three independent experiments. (F) Quantification of RE tubule density (number of RE tubules per cell) for KIF13A WT and ΔP motors. (G) Average length of RE tubules in cells expressing KIF13A WT or ΔP. Data presented as means ± SD calculated using Student's *t* test (****P* < 0.001). (H) Plot showing recycling dynamics of KIF13A WT and ΔP motors. Average CTCF (corrected total cell fluorescence) values presented as means ± SEM (*****P* < 0.0001). *n* indicates the number of cells considered for each analysis. Yellow dotted lines indicate the cell boundary, and asterisk indicates the nucleus. Scale bars, 10 μm. a.u., arbitrary units.

RESULTS

KIF13A WT and ΔP390 motors manifest distinct RE phenotype in cells

WT KIF13A has been reported to be involved in generation of RE tubules and cargo recycling *in vivo* (5, 6, 26). Therefore, we wanted to know whether constitutively active KIF13A ΔP motor forms RE tubules similar to WT KIF13A (Fig. 1, A and B). *In vivo* expression of C-terminal mCitrine (mCit)-tagged KIF13A WT and ΔP motors resulted in distinct RE phenotypes. Expression of KIF13A WT motor resulted in a dense network of cytoplasmic tubular REs (Fig. 1B and movie S1), consistent with previous works (6, 26). In contrast,

expression of ΔP motor displayed largely vesicular REs accumulated at the cell periphery rather than tubular REs (Fig. 1C and movies S2 and S3). We wanted to confirm that this alteration in morphology and distribution of REs did not affect colocalization of ΔP motors with REs. Therefore, we coexpressed KIF13A WT or ΔP motors with well-established RE (syntaxin 13 and transferrin), sorting endosome (EEA1) and lysosome [lysosomal-associated membrane protein 1 (LAMP1)] markers (6, 26, 33, 34). These KIF13A-labeled tubular and vesicular REs showed strong colocalization with syntaxin 13 and internalized transferrin, but not with EEA1 and LAMP1 (fig. S1, A to D, and table S1). Since KIF13A colocalizes strongly with syntaxin 13, a well-known RE marker, we considered KIF13A as readout of REs for this study.

Next, to characterize the observed phenotypic differences in WT and ΔP motors, we manually quantified three different parameters of RE tubulation: (i) efficiency, percent transfected cells displaying RE tubulation; (ii) density, number of RE tubules per cell; and (iii) length, average length of RE tubules. Expression of ΔP resulted in a remarkable decrease in efficiency of RE tubulation (~50%), RE density, and tubule length as compared with WT motor (Fig. 1, D to G, and table S1). Correspondingly, a marked increase was observed in percent cells showing vesicular REs accumulating at the cell periphery. These phenotypic differences led us to wonder whether their physiological function (cargo recycling) is also affected in these cells. Kinetic analysis of functional transferrin assay showed no difference in the transferrin uptake (fig. S1E). However, a significantly faster recycling of transferrin was observed for ΔP motors compared with WT (Fig. 1H). The phenotypic and physiological differences observed between WT and ΔP suggest a critical role of proline in KIF13A-associated RE tubulation and cargo recycling. This prompted us to ask whether the observed disparity in RE phenotype is the result of a difference in motility parameters between KIF13A WT and ΔP motors.

Proline between NC-CC1 domains of KIF13A determines RE transport properties

Before analyzing the motility dynamics of KIF13A, we wanted to confirm that MTs are major means of RE transport and tubulation. KIF13A-labeled tubular and vesicular REs displayed dynamic motion along MT tracks that are labeled with green fluorescent protein (GFP)-α-tubulin (fig. S1F and movie S4). Thus, nocodazole-induced MT disruption in cells expressing WT or ΔP motors resulted in a loss of RE tubulation or peripheral accumulation of RE vesicles, respectively (fig. S1G and movies S5 and S6), but not with solvent dimethyl sulfoxide (DMSO) control. This suggests that these phenotypic differences are MT-dependent.

A potential reason for distinct RE phenotypes between WT and ΔP could be due to differences in their motility properties. To test this, we performed total internal reflection fluorescence (TIRF) live-cell RE transport analysis of KIF13A WT and ΔP motors. Such analysis requires prior knowledge of MT polarity. Expression of fluorescently tagged EB3, an MT plus-end tracking protein, confirmed a distinct MT organization with minus-ends near the nucleus and plus-ends extending radially toward the cell periphery (movie S7) (22). Hence, the outward-directed motion of REs is driven by KIF13A and accounted them for analysis. Following this, we analyzed individual KIF13A WT-labeled tubular and vesicular RE transport properties frame by frame using custom-written ImageJ plugin. KIF13A WT-labeled tubular REs extended gradually with an average

velocity of $0.46 \pm 0.01 \mu\text{m/s}$ over long distances ($\sim 9 \mu\text{m}$) (Fig. 2A, table S2, and movie S1) and showed intermittent sudden retractions (fig. S2A). Similarly, KIF13A WT-labeled vesicular REs showed uniform long runs ($\sim 10 \mu\text{m}$) with frequent reversals (fig. S2B). Average

velocity of these vesicles was found to be $1.06 \pm 0.11 \mu\text{m/s}$ (Fig. 2B and table S2), which is twice the speed of WT motors pulling RE tubules.

Compared with WT, only a small population of cells expressing ΔP motors generated RE tubules. Furthermore, the number of RE

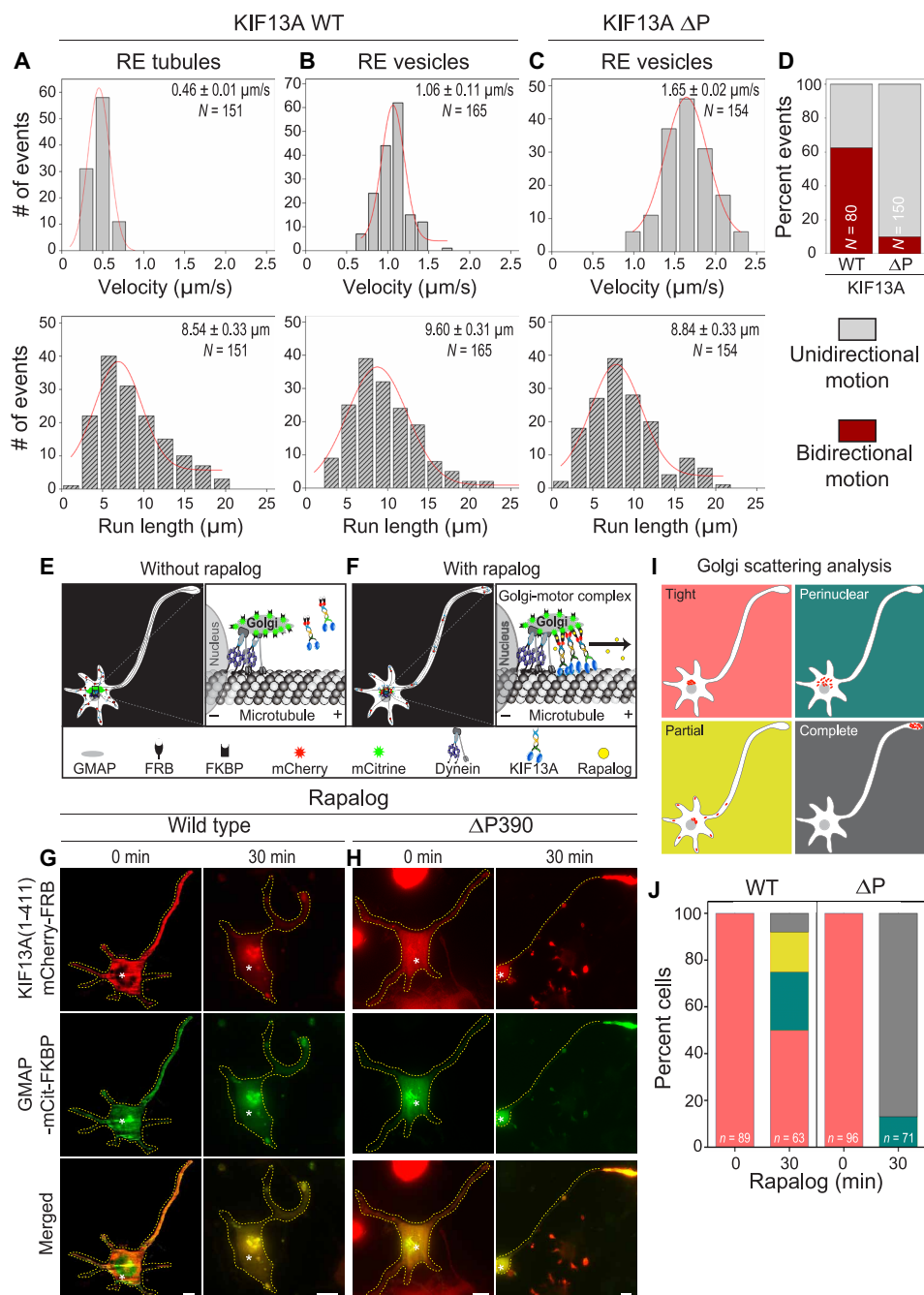


Fig. 2. KIF13A WT and ΔP manifest distinct dynamics in vivo. (A to C) Quantification of in vivo cargo transport properties for KIF13A WT, tubular (A) and vesicular REs (B), and KIF13A ΔP vesicular REs (C). Manual tracking was performed, and histograms for velocities (top) and run lengths (bottom) were plotted; Gaussian distribution was fit. (D) Percent vesicles showing unidirectional/bidirectional motion for WT and ΔP motors. Mean velocity \pm SEM indicated at top right; N , number of events. Note that intermittent pauses and retraction were not considered while measuring velocity and run length. (E and F) Schematic of Golgi scattering assay in differentiated CAD cells. Motors are tagged with mCherry-FRB [KIF13A(1-411)-mCherry-FRB or KIF13A(1-411 ΔP)-mCherry-FRB], and Golgi is labeled with GMAP-mCit-FKBP (E). Rapalog treatment recruits motor to Golgi (F). Magnified view of area marked in (E) and (F) showing motor dynamics on Golgi to their right. (G and H) Differentiated CAD cells expressing KIF13A(1-411) (G) and KIF13A(1-411 ΔP) (H). Images captured at 0 and 30 min after rapalog treatment. (I and J) Cartoon (I) depicting categories used for quantification (J) of Golgi scattering at 0 and 30 min after rapalog treatment. n indicates number of cells. Yellow dotted lines indicate the cell boundary, and asterisks indicate the nucleus. Scale bars, $10 \mu\text{m}$.

tubules per cell in this population was much less than the WT. These RE tubules showed highly dynamic motion and rapid fragmentation into vesicles that were transported to the cell periphery (movies S2 and S3). Therefore, we could not measure RE tubule dynamics for ΔP motors. Nonetheless, vesicular REs transported by ΔP showed robust unidirectional long motion ($\sim 9 \mu\text{m}$), with higher velocity ($1.65 \pm 0.02 \mu\text{m/s}$) compared with WT motor (Fig. 2C and fig. S2C). Furthermore, a considerable decrease ($>35\%$) was observed in the percentage of vesicles showing reversals in ΔP motors, as compared with WT (Fig. 2D). Together, these results indicate that observed differences in RE phenotype between WT and ΔP are due to their distinct transport properties, suggesting a crucial role of proline in regulating motor activity and, hence, RE tubulation.

RE tubulation requires action of MT-associated motor proteins

Membrane tubulation and elongation of cellular organelles depend on the interplay between MT-based opposite-polarity motors, dynein, and kinesin (16, 35–38). To test this hypothesis, we disrupted the function of dynein and KIF13A independently and analyzed the effect on RE tubulation. To block dynein activity, we first overexpressed p50 dynamitin, which inhibits dynein function by disrupting the dynein-dynactin complex (39). Thus, cells coexpressing either KIF13A WT or ΔP motor with dynamitin showed marked decrease ($>80\%$) in cytoplasmic RE tubules and led to accumulation of RE vesicles at the cell periphery (fig. S2, D, I, and J). Next, we treated cells expressing KIF13A WT or ΔP motors with an inhibitor of dynein ATPase activity, ciliobrevin D, which is critical for motor function along the MT (40). Treatment with ciliobrevin D also showed a complete loss of RE tubules in the cytoplasm (fig. S2, E, I, and J) and clustered RE vesicles at the cell periphery.

Similarly, disruption of KIF13A function by expressing headless [KIF13A(359-1750)] or an MT binding-deficient mutant [KIF13A(T104I)] failed to induce tubular REs (fig. S2, F, G, I, and J). Instead, they predominantly showed vesicular REs distributed in the cytoplasm. In addition, we generated a KIF13A NC dimerization-deficient mutant (NC mutant) by replacing the hydrophobic residues at the “a” and “d” positions of NC with charged residues, as described for *CeUNC-104* and KIF16B (15). The expression of NC mutant also failed to generate RE tubules and showed perinuclear clustering of RE vesicles (fig. S2, H to J). Together, the data support that the interplay between KIF13A and dynein along MTs is indispensable for RE tubulation.

Proline hinders KIF13A force generation in vivo

The ability of ΔP motors to disrupt RE tubules into vesicles and transport them at higher velocities hinted at the possibility of higher force generation compared with WT. To test this, we targeted WT and ΔP motors to Golgi, a non-native cargo of KIF13A, using the Golgi-targeting sequence of HsGMAP210 and challenged their ability to scatter Golgi. In general, Golgi is a clustered perinuclear organelle tightly held by the combined activity of multiple cytoplasmic dyneins, myosins, and associated proteins. Disruption of Golgi from its tight perinuclear-to-scattered morphology requires 100 to 200 pN of opposite forces and, thus, is considered a heavy load cargo (19). Active motors that can generate higher force disrupt Golgi and transport them to plus-ends of MTs and accumulate at the cell periphery, whereas weak or inactive motors fail to generate higher force required for Golgi disruption, resulting in intact Golgi (Fig. 2, E and F

(15). Therefore, Golgi scattering assay is considered a direct readout of in vivo force generation by motors: The higher the scattering, the higher the force. To target KIF13A motors to the Golgi complex, we used chemically inducible FKBP/FRB (FK506-binding protein/FKBP-rapamycin binding) heterodimerization system (19, 41, 42). We labeled the Golgi with the Golgi-targeting sequence from HsGMAP210 fused to mCit and FKBP, a binding partner of FRB in the presence of rapamycin (GMAP210-mCit-FKBP) (43). Next, we tagged the C-terminal region of WT KIF13A(1-411) or KIF13A(1-411 ΔP) motors with mCherry-FRB (FKBP12-rapamycin binding domain).

As expected, CAD (Cath.-a-differentiated) cells expressing KIF13A(1-411) or KIF13A(1-411 ΔP) showed intact Golgi complex near the nucleus (Fig. 2, G and H). Treatment of CAD cells expressing KIF13A(1-411) or KIF13A(1-411 ΔP) with rapalog, an analog of rapamycin, rapidly induced the recruitment of motors to the Golgi complex (Fig. 2, G and H). CAD cells expressing KIF13A(1-411) WT showed only a small population of cells ($\sim 10\%$) with scattered Golgi and its accumulation at neurite tips (Fig. 2, G, I, and J). In contrast, $\sim 90\%$ of the cells expressing KIF13A(1-411 ΔP) induced robust Golgi scattering and accumulation at neurite tips (Fig. 2, H to J, and fig. S3). Similar analysis in COS-7 (fig. S4, A to F) and HeLa (fig. S4G) cells showed consistent results. Overall, these results clearly indicate that ΔP motors are able to generate higher force compared with WT, explaining loss of RE tubules and robust transport of RE vesicles to the cell periphery. However, the lesser force exerted by WT motor is counterbalanced by dynein, essential for RE tubulation.

Rab10/Rab22A enhance KIF13A-mediated RE tubules

Neither KIF13A inactive monomer nor constitutively active ΔP dimer can form RE tubules, suggesting that KIF13A WT motor falls somewhere between these two extremes to generate RE tubules in vivo. Therefore, we investigated the cellular mechanism that relieves the proline-induced kink between NC-CC1 and supports KIF13A motor dimerization and RE tubulation. Recent studies have shown that certain Rab proteins directly interact with KIF13A and play important roles in RE tubulation and cargo recycling (5, 6, 26). We, thus, examined the effect of different Rab proteins (Rab8A, Rab7A, Rab10, Rab11A, Rab22A, and Rab35A) on KIF13A WT- and ΔP -induced REs (5, 6, 12, 26, 38).

Expression of KIF13A WT or ΔP motors showed varied colocalization signals with different Rab proteins. Rab8A, Rab11A, Rab10, and Rab22A recorded a moderate-to-high degree of codistribution, whereas Rab7A and Rab35A displayed poor codistribution (table S1). Cells coexpressing KIF13A WT with different Rabs exhibited a notable variation in the morphology and distribution of REs (Fig. 3A). To quantitatively appreciate the observed variations, we analyzed three different parameters: (i) efficiency, (ii) density, and (iii) length of RE tubulation, as mentioned for Fig. 1 (D to G). Among the Rabs tested, Rab10 and Rab22A boosted the RE tubulation efficiency ($>20\%$) and density ($>50\%$) (Fig. 3, B and D). In contrast, coexpression of KIF13A with Rab7A, Rab8A, Rab11A, or Rab35A revealed a decreased RE tubulation. However, no marked difference in the average length of RE was noted as compared with cells expressing the motor alone (Fig. 3E). As expression of ΔP alone exhibited a notable decrease in RE tubulation, its coexpression with different Rabs showed only a small effect on RE morphology and distribution (fig. S5). Furthermore, coexpression of KIF13A WT or ΔP with constitutively active Rab10^{Q68L} or Rab22A^{Q64L} showed a strong RE

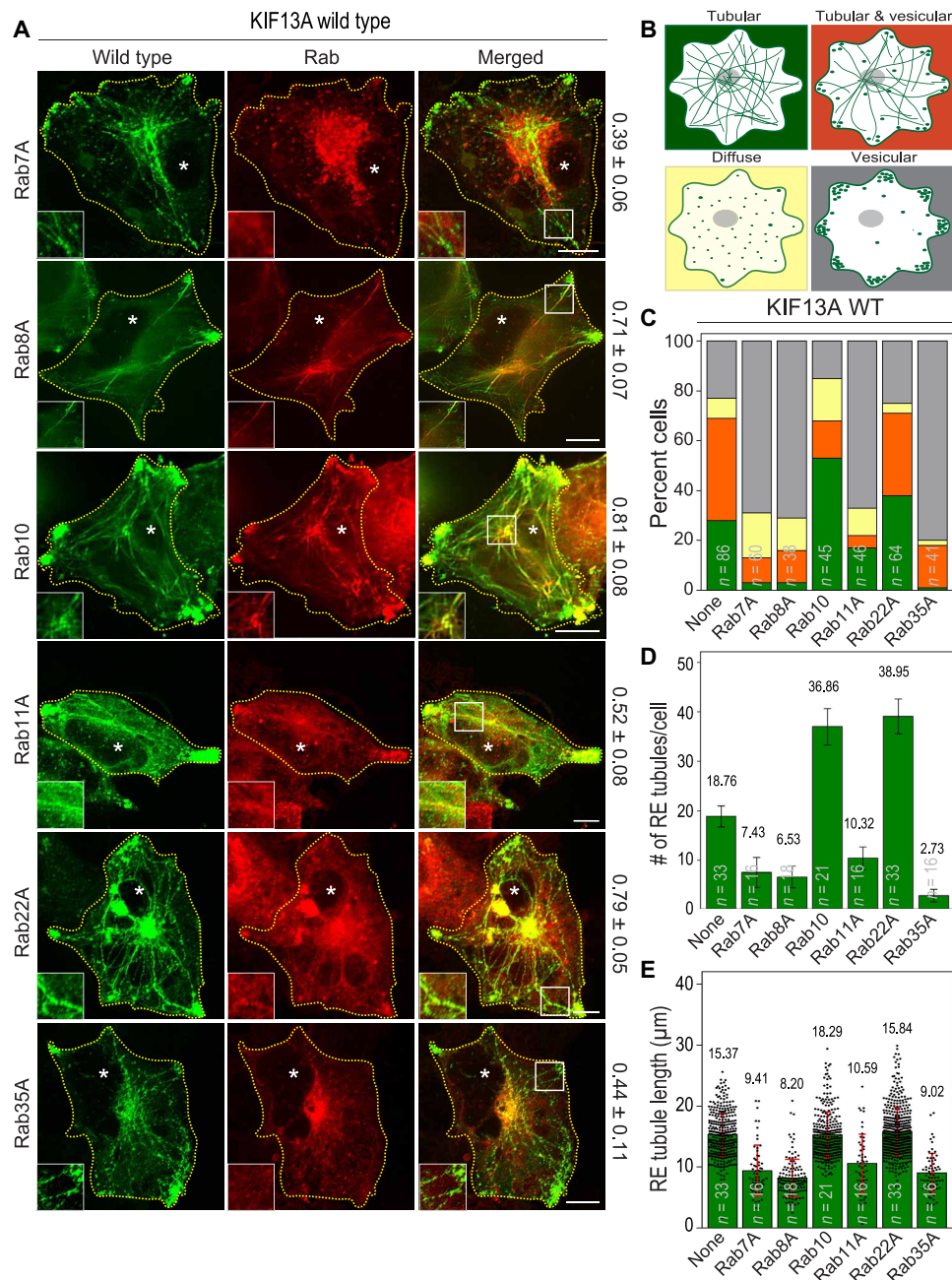


Fig. 3. Rab10/Rab22A augment KIF13A RE tubulation. (A) Coexpression of KIF13A WT with all six Rabs (Rab7A, Rab8A, Rab10, Rab11A, Rab22A, and Rab35A) in HeLa cells. Corresponding PCC values indicated on the right as means ± SD. Insets show magnified view of area marked with square. (B and C) Cartoon diagram (B) depicting categories for quantification of RE tubulation (C) for WT with all Rabs. RE tubule density for KIF13A WT (D) in the presence of different Rabs. Average RE tubule length for KIF13A WT (E) with Rab proteins. Data from three independent experiments presented as means ± SD. Value indicated above each bar is mean RE density. *n* indicates the number of cells considered for each analysis. Yellow dotted lines indicate the cell boundary, and asterisks indicate the nucleus. Scale bars, 10 µm.

localization and increased RE tubulation (figs. S6 and S7). In contrast, coexpression with dominant-inactive Rab10^{T23N} or Rab22A^{S19N} caused a marked decrease in RE tubulation (figs. S6 and S7). Analysis of fluorescence intensity of the expressed Rab protein to the number of RE tubules on a cell-by-cell basis suggested that KIF13A-mediated RE tubulation is dependent on Rab22A concentration in cells (fig. S7G).

Although Rab11A has been reported to interact with KIF13A, a decrease in RE tubulation efficiency presumably suggests its importance in later stages of cargo recycling (fig. S8) (8, 9). In line with observed low-to-moderate colocalization signals, analysis of Rab7A, Rab8A, and Rab35A revealed a marked decrease in efficiency, density, and length of RE tubules when compared with cells expressing motor alone, and therefore, we did not investigate them further.

Collectively, these results indicate that the GTP-bound form of Rab10 and Rab22A plays vital roles in RE tubulation (5, 6).

Headless KIF13A generates RE tubules only with Rab22A

To decipher the specific KIF13A domains involved in RE tubulation with Rab10 and Rab22A, we generated KIF13A dominant-negatives (359-1750, 450-1750, 640-1750, 775-1750, and 1130-1750) (Fig. 4A). We hypothesized that motors without catalytic MD will not be able to generate RE tubules, even in the presence of Rab protein. Consistent with this, expression of these dominant-negatives alone or coexpression with Rab10 or Rab11A failed to generate RE tubules and showed vesicular REs in the cytoplasm (Fig. 4A and figs. S9 and S10). Unexpectedly, except 1130-1750, all dominant-negatives formed RE tubules upon coexpression with Rab22A^{WT} or Rab22A^{Q64L} (Fig. 4B and figs. S9 and S10). In contrast, Rab22A^{S19N} failed to form RE tubules when coexpressed with any of the KIF13A dominant-negatives (Fig. 4B and figs. S9 and S10). To rule out the possibility that other Rabs might generate RE tubules with KIF13A dominant-negative,

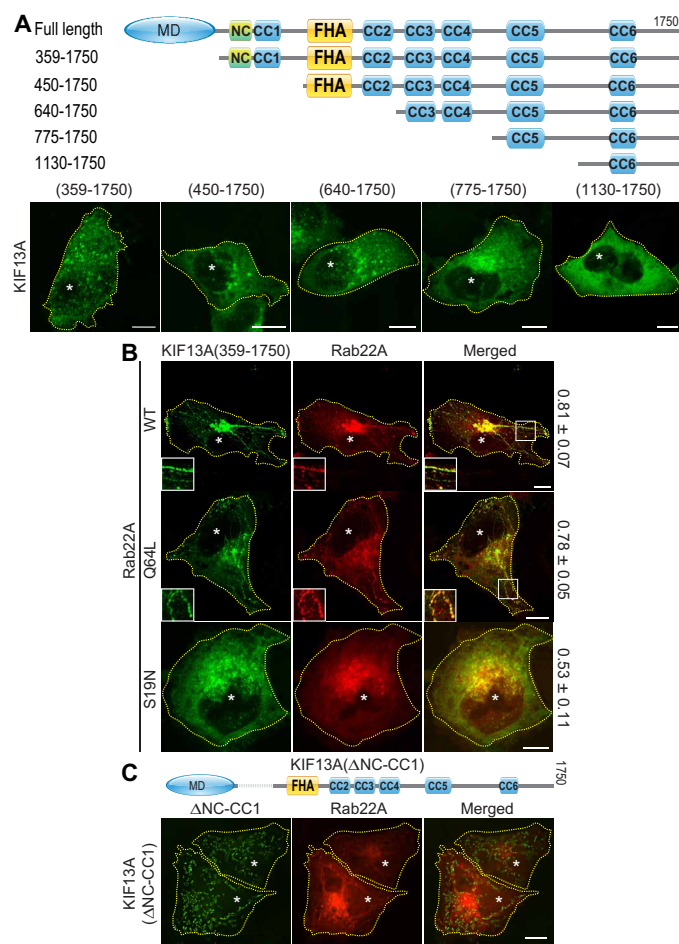


Fig. 4. KIF13A dominant-negatives induce RE tubulation only with Rab22A.

(A) KIF13A dominant-negatives used in this study. Expression of individual KIF13A dominant-negatives in HeLa cells. (B) Coexpression of KIF13A(359-1750) with WT (Rab22A^{WT}), GTP-bound constitutively active form (Rab22A^{Q64L}), and GDP-bound dominant-negative form (Rab22A^{S19N}). Corresponding PCC values indicated on the right as means ± SD. Insets show magnified view of area marked with square. (C) Coexpression of KIF13A(ΔNC-CC1) with Rab22A in HeLa cells. Yellow dotted lines indicate the cell boundary, and asterisks indicate the nucleus. Scale bars, 10 μm.

we coexpressed KIF13A(359-1750) with all six Rabs (fig. S9A). Of all the Rabs tested, only Rab22A led to RE tubulation when coexpressed with KIF13A dominant-negatives (fig. S9). The ability of headless KIF13A to form RE tubules with Rab22A was unexpected, because catalytic activity of KIF13A MD is critical for taking progressive steps along the MT to generate RE tubules (26). Notably, dominant-negatives generated after NC-CC1 showed a decrease in RE tubulation when coexpressed with Rab22A, indicating a possible interaction between Rab22A and NC-CC1 (fig. S9, B and C). To further appreciate the importance of NC-CC1 domains in RE tubulation, we created an NC-CC1 deletion mutant of KIF13A [KIF13A(ΔNC-CC1)], which failed to generate RE tubules even in the presence of Rab22A (Fig. 4C). Instead, it formed short membranous structures that failed to colocalize with Rab22A and displayed diffusive motion in the cytoplasm (movie S8). In addition, we coexpressed KIF13A WT or NC mutant (L370K/V374G) (fig. S2H) with Rab22A in HeLa cells. Coexpression of KIF13A NC mutant with Rab22A showed no RE tubulation, compared to KIF13A WT with Rab22A (fig. S11). These findings clearly demonstrate that both catalytic activity of KIF13A MD and interplay between Rab22A and NC-CC1 domains are crucial for RE tubulation. These results also imply that Rab22A presumably binds to the NC-CC1 domains and favors RE tubulation.

Rab22A directly binds to NC-CC1 domains in a nucleotide-dependent manner

To further verify the interactions observed in coexpression studies between KIF13A and Rabs, we performed biochemical pull-down experiments using purified Rab proteins and individual KIF13A domain fragments: NC-CC1 (359-436), FHA-CC2 (469-640), CC3-CC4 (653-772), and CC5 (1099-1140). These experiments revealed that Rab22A^{WT} and constitutively active Rab22A^{Q64L} bind directly to all domain fragments, including NC-CC1 (fig. S12, A to C). We further tested whether deletion of proline alters binding ability of Rab22A to NC-ΔP-CC1. Rab22A showed enhanced binding to NC-ΔP-CC1 [dissociation constant (K_d) = $5.99 \pm 0.39 \mu\text{M}$], compared with NC-CC1 (K_d = $12.26 \pm 0.76 \mu\text{M}$) (fig. S12, D and E), indicating that proline-induced kink between NC-CC1 hinders Rab22A binding. Deletion of this proline opens up the α helix, allowing better access to Rab22A and thereby resulting in its stronger binding to NC-ΔP-CC1. We further analyzed whether disruption of NC-CC1 dimerization affects Rab22A interaction. We found that similar to WT NC-CC1, Rab22A retained its binding to NC mutant (L370K/V374G) (fig. S12F). We also checked interaction of KIF13A domain fragments with Rab10 and Rab11A, since they have been previously reported to interact with KIF13A (5, 6, 26). Consistent with previous work (5), Rab10 showed binding only to CC5 domain in its active GTP-bound form (fig. S12, G and H). Rab11A showed binding to CC3-CC4 domains in GTP-bound form (fig. S12, I and J). Together, these results suggest that only Rab22A binds to the NC-CC1 domains, and this interaction is crucial for motor dimerization and RE tubulation in vivo.

Rab22A interaction enables NC-CC1 dimerization of KIF13A

We hypothesized that direct binding of Rab22A relieves proline-induced kink and enables dimerization of NC-CC1. To test this hypothesis, we took advantage of the fact that KIF13A WT motors are monomers, whereas the ΔP motors are strong dimers in vitro (15). Since NC-CC1 domains play a crucial role in motor dimerization,

we decided to determine the effect of Rab22A on the oligomeric state of NC-CC1 and NC- Δ P-CC1 in vitro, using bimolecular Förster resonance energy transfer (FRET) assay. This technique is highly sensitive to the distance between donor and acceptor. Therefore, we generated NC-CC1 and NC- Δ P-CC1 FRET sensors having either FRET donor mCerulean (mCer) or FRET acceptor mCit at the C terminus to measure proximity interactions between KIF13A domain fragments. These FRET sensors and Rab22A were purified from insect cell expression system and used for FRET emission measurement.

For WT NC-CC1, low basal FRET was observed (Fig. 5, A and B), suggesting that it exists in a monomeric state due to proline-induced intramolecular interaction between NC and CC1 domains. Addition of Rab22A^{WT} or Rab22A^{Q64L}, but not Rab22A^{S19N}, to NC-CC1 fragments resulted in a significant increase in the FRET ratio (Fig. 5 A and B), demonstrating that binding of active Rab22A relieves the proline-induced kink and favors the intermolecular NC-CC1 di-

merization. In contrast, NC- Δ P-CC1 fragments alone exhibited significantly higher FRET (Fig. 5, C and D), suggesting that they exist as dimers. Therefore, addition of Rab22A or its mutants did not considerably alter FRET ratio (Fig. 5, C and D). These results are in agreement with our previous single-molecule motility assays, in which WT motors [KIF13A(1-411)-3xmCit] exist in a monomeric state and show no processive motility, whereas proline deletion motors [KIF13A(1-411 Δ P390)-3xmCit] exist in a dimeric state and show superprocessive motility (15).

Together, these results clearly demonstrate that proline at the junction of KIF13A NC-CC1 favors intramolecular NC-CC1 interaction and inhibits intermolecular dimerization. On the contrary, binding of Rab22A stabilizes the helix and endows intermolecular motor dimerization. Deletion of proline alone is sufficient to eliminate the kink between NC-CC1 domains that results in a stable straight helix and enables strong motor dimerization.

Binding of Rab22A converts inactive KIF13A monomers into processive dimers

As Rab22A binding enabled NC-CC1 dimerization (Fig. 5, A and B), we questioned whether this will allow WT KIF13A to be processive. To test this, we performed in vitro single-molecule motility assays using TIRF microscopy. Consistent with previous studies, truncated WT KIF13A(1-411) exist as monomers and did not show processive motility (fig. S13A) (15). When incubated with Rab22A^{WT} or constitutively active Rab22A^{Q64L}, WT KIF13A(1-411) showed an MT-based long processive motility (4.99 ± 0.14 and 6.94 ± 0.19 μ m), with a speed of 0.83 ± 0.01 and 0.96 ± 0.01 μ m/s, respectively (Fig. 5, E and F; fig. S13, B and C; and table S2). In contrast, KIF13A(1-411) motors incubated with dominant-inactive Rab22A^{S19N} did not show any MT-based motion, except for few slow and short runs (Fig. 5G, fig. S13D, and table S2).

As KIF13A(1-411 Δ P) exist as dimers and showed MT-based superprocessive motility (10.14 ± 0.27 μ m), with an average speed of 1.47 ± 0.01 μ m/s (Fig. 5H, fig. S13E, and table S2) (15), addition of Rab22A^{WT} or constitutively active Rab22A^{Q64L} did not alter its motility properties. A comparative analysis of landing rates of these motors on MTs showed highest number of events (~ 47 events/ μ m MT/min) for KIF13A(1-411 Δ P). However, KIF13A(1-411) showed moderate number of landing events only in the presence of Rab22A^{WT} (~ 12 events/ μ m MT/min) and Rab22A^{Q64L} (~ 18 events/ μ m MT/min) (fig. S13F). As expected, KIF13A(1-411) showed negligible number of landing events (~ 3 events/ μ m MT/min) in the presence of Rab22A^{S19N} (fig. S13F). Together, these results support our hypothesis that Rab22A regulates the oligomeric state and processive cargo transport properties of KIF13A in vivo.

DISCUSSION

An important feature that distinguishes KIF13 motors from other kinesin-3 family members is the presence of a conserved proline at the NC-CC1 α -helical junction across species, with exception of the *Caenorhabditis elegans* homolog KLP (Kinesin-Like Protein)-4 (15). Because of the steric effect, proline is one of the least likely amino acids found in the α helix core, present either at the start or at the end of the helix. If present, it often kinks or breaks the helix, as observed in KIF13A (15, 27, 28). Evolutionary presence and physiological relevance of proline in KIF13A require investigation of motor function on its native cargo in vivo. Such analysis has been limited

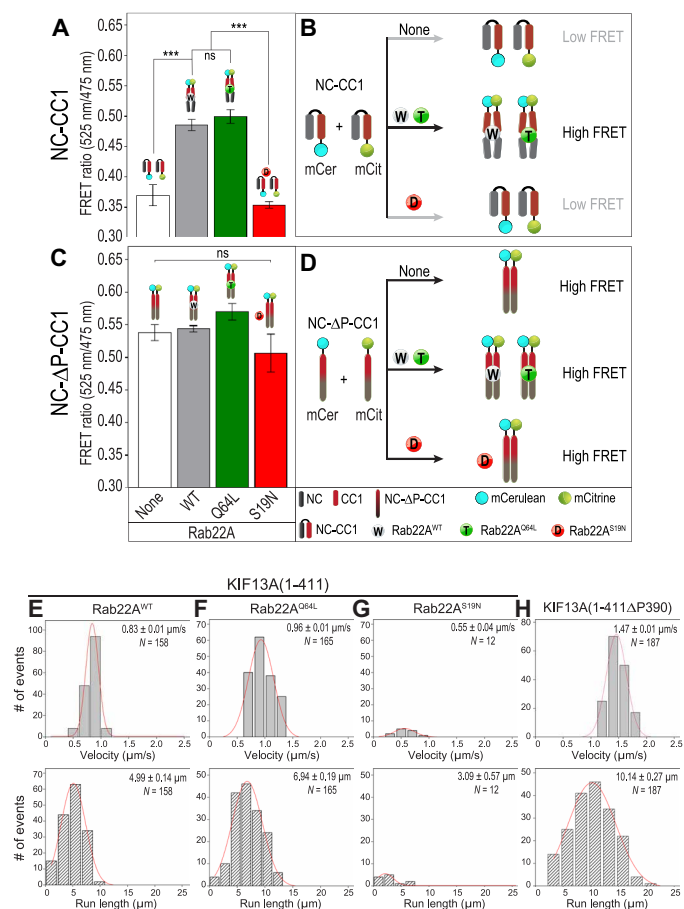


Fig. 5. Direct binding of Rab22A favors KIF13A NC-CC1 dimerization and processive motility. (A to D) FRET ratio for NC-CC1 (A) and NC- Δ P-CC1 (C) in the absence/presence of Rab22A^{WT}, Rab22A^{Q64L}, or Rab22A^{S19N}. Respective schematic representations are shown in (B) and (D). Error bars represent means \pm SD. Statistical difference calculated using Student's *t* test (***) $P < 0.001$; ns, nonsignificant. (E to H) In vitro TIRF single-molecule motility assays using COS-7 cell lysates of KIF13A(1-411) with Rab22A^{WT} (E), Rab22A^{Q64L} (F), Rab22A^{S19N} (G) and KIF13A(1-411 Δ P) (H). Histograms for velocity (top) and run length (bottom), fit to a Gaussian distribution. Average velocity and run length of the corresponding population of motors (*N*) are indicated on the top right corner as means \pm SEM. Values from three independent experiments.

previously, since full-length motors exist in monomeric inactive state (14, 15). As compared with KIF13A Δ P motors, WT KIF13A displayed substantially decreased velocity and force, presumably due to proline-induced steric hindrance in the NC-CC1 domains, resulting in weak motor dimerization. These observations agree with previous studies, which reported that the NC domain of KIF1A/UNC-104 and kinesin-73 have weak propensity to form dimeric motor and display slower velocity and short processive runs along the MT in vitro (15, 44–46). However, fusion of leucine zipper fragment or kinesin-1 NC domain to truncated KIF1A or kinesin-73 converted weak NC dimer into strong stable dimer and resulted in robust superprocessive motility, similar to KIF13A Δ P motor (15, 44–46). Together, our results support a general model in the field: NC-mediated stable dimerization is essential for a dimeric motor to produce robust processive motility and exert maximum force. Therefore, we concluded that the presence of proline hinders intermolecular motor dimerization to regulate RE tubulation.

RE tubules displayed characteristic features of molecular tug-of-war: membrane elongation, slower velocity, and occasional fission, indicating that kinesin (KIF13A) and dynein apply force against each other (16, 35). The tug-of-war model suggests action between teams of opposite-polarity motors with asymmetry in their motor number, strength, and tenacity (16). However, our data suggest that RE tubulation requires action between teams of oppositely directed motors, with similar properties, which exert forces close to equilibrium. Therefore, an altered equilibrium, in favor of either anterograde kinesin or retrograde dynein, resulted in a complete loss of RE tubules. Besides, we found a substantial decrease in the percentage of events, showing bidirectional motion for KIF13 Δ P, when compared with KIF13A WT motors, due to this altered equilibrium. On the basis of this evidence, we propose that RE tubules act like a

spring: Dyneins at static end near nucleus exert opposite force on KIF13A at the dynamic end, extending RE tubules toward the cell periphery. As a result, KIF13A motors at the leading edge presumably experience a higher backward force that can notably decrease their velocity and increase MT detachment rates. Since Δ P motors generate higher force and velocity, they alter this equilibrium and win tug-of-war against dynein (16). On the basis of these findings, we conclude that the RE tubulation is a result of near-balanced opposite forces exerted by KIF13A and dynein in a molecular tug-of-war. Our research provides an ideal in vivo system that can be exploited to study the mechanism of tug-of-war between teams of opposite-polarity motor proteins.

In general, Rab proteins regulate recruitment of motors onto membranes and achieve intracellular trafficking (26, 33, 47–52). During recycling endocytosis, binding of Rab10 to the C terminus of KIF13A presumably recruits monomeric motors to the cargo (5). Next, Rab22A binds to NC-CC1 domains, relieves proline-induced inhibition, and enables motor dimerization and RE tubulation. Thus, Rab22A can be considered as a molecular switch between two states of KIF13A on REs: inactive and active (Fig. 6). In the inactive state, motor exists as monomers in folded conformation due to proline-mediated kink between NC and CC1 domains (Fig. 6A). In the active state, binding of Rab22A to the NC-CC1 of KIF13A relieves proline inhibition and allows motor dimerization and motility to generate balanced opposite force against dyneins, resulting in RE tubulation (Fig. 6B). Conversely, disruption of this regulation in Δ P results in a stable constitutive dimer (Fig. 6C) that can generate robust motility and higher force, allowing Δ P to fragment RE tubules into vesicles and transport them to the cell periphery (movies S2 and S3), independent of Rab22A (Fig. 6D). In summary, we demonstrate that cargo-bound KIF13A motors function as weak dimers

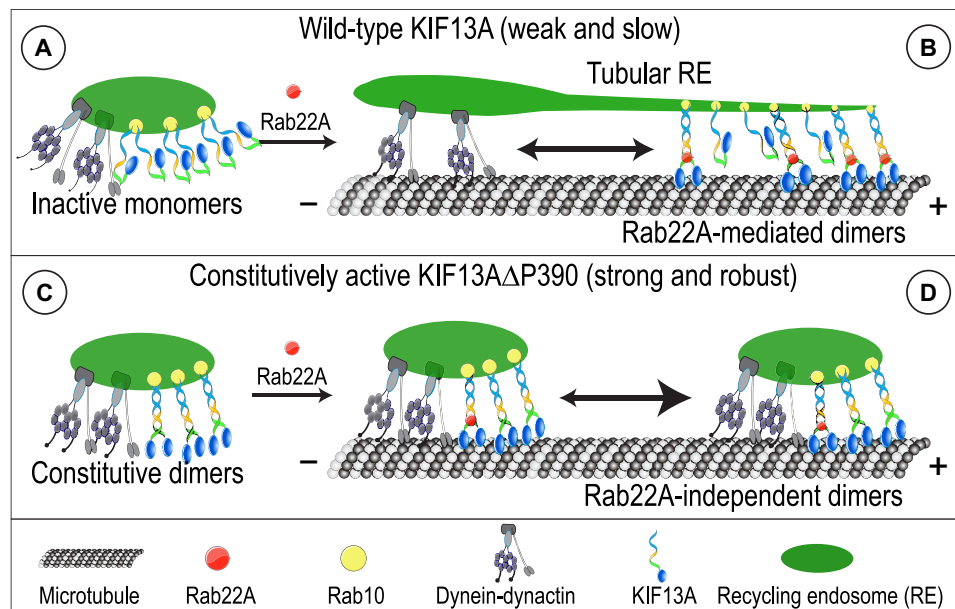


Fig. 6. Rab22A, a molecular switch that regulates KIF13A to function as weak dimers in vivo. (A to D) Proline (P390)-mediated inhibition in WT KIF13A forestalls motor activity and retains the motor in an inactive monomeric state (A). During the RE tubulation, binding of Rab10 to the C-terminal tail of KIF13A recruits motor to the cargo. Subsequent binding of Rab22A to NC-CC1 relieves the inhibition, facilitating motor dimerization and activation, critical for cargo transport. In a near-balanced tug-of-war between KIF13A and dynein, REs are manifested as dynamic tubular structures (B). However, when this regulatory proline is removed (Δ P390), KIF13A motors exist as constitutively active strong dimers (C), independent of Rab22A binding. Higher force exerted by KIF13A Δ P390 ruptures tubular REs into vesicles and transports them to the cell periphery (D).

that are regulated by Rab22A, critical for RE biogenesis and endocytic cargo recycling.

Several Rab proteins have been shown to colocalize and mediate binding of motor proteins to the REs, but only few bind motors directly (53), and none bind to motor dimerization domain and regulate motor activity. Therefore, regulatory mechanism of Rab22A binding to NC-CC1 domains of KIF13A represents a unique model that has important consequences in KIF13A cellular functions. To our knowledge, this is the first report of a Rab-mediating motor dimerization and subsequent activation of motor on the cargo.

In conclusion, we propose a unique mechanism of RE tubule dynamics that is dependent on Rab22A-mediated activity of KIF13A. This work will provide molecular basis for understanding the anomalies of motor-Rab interactions during specific disease conditions. Further work is necessary to understand the hierarchy and interplay of different Rabs and motor proteins during various stages of endocytosis.

MATERIALS AND METHODS

Reagents and plasmids

All reagents were purchased from Sigma-Aldrich, Bengaluru, India, unless stated otherwise. All the antibodies used in the present study were purchased from Thermo Fisher Scientific, India.

6xHis-Rab22A^{WT}-pET28a⁺, 6xHis-Rab22A^{Q64L}-pET28a⁺, 6xHis-Rab22A^{S19N}-pET28a⁺, mCherry-Rab7A, mCherry-Rab11A, mCherry-Rab22A^{WT}, mCherry-Rab22A^{Q64L}, and mCherry-Rab22A^{S19N} are the same as used in (6). 6xHis-Rab11A^{WT}, 6xHis-Rab11A^{Q70L}, and 6xHis-Rab11A^{S25N} were generated by cloning into pET28a⁺ via the Bgl II and Bam HI sites. KIF13A domain fragments were polymerase chain reaction (PCR) amplified from KIF13A-mCit and cloned into pGEX-4T3 using Eco RI and Xho I restriction enzyme sites. Dominant-negative constructs of KIF13A were PCR amplified and cloned into mCit-N1 vector using Nhe I and Acc 65I sites. All other plasmids, such as mCherry-LAMP1, red fluorescent protein (RFP)-EB3, and fluorescent backbone plasmids, were a gift from K. Verhey (University of Michigan, USA).

Rab22A-mCit was generated by cloning Rab22A into mCit-N1 vector via the Age I and Bsr GI sites. Rab11A^{Q70L} and Rab11A^{S25N} were generated by using QuikChange site-directed mutagenesis kit (Agilent). Rab8A-mCherry was generated by cloning Rab8A into mCherry-N1 via the Nhe I and Hind III restriction enzyme sites. Enhanced GFP (EGFP)-Rab10^{WT}, EGFP-Rab10^{Q68L}, and EGFP-Rab10^{T23N} plasmids were a gift from M. Fukuda (Tohoku University, Japan). Rab10^{WT}, Rab10^{Q68L}, and Rab10^{T23N} were cloned into pET28a⁺ vector backbone using Eco RI and Xho I restriction enzyme sites. Similarly, Rab10^{WT}, Rab10^{Q68L}, and Rab10^{T23N} were cloned into mCherry-N1 vector using the Bsr GI and Mfe I sites.

KIF13A-mCit and KIF13A(Δ P390)-mCit constructs were according to (15). QuikChange site-directed mutagenesis kit (Agilent) was used to create KIF13A(T104I)-mCit and KIF13A(L370K/V374G)-mCit. KIF13A(Δ NC-CC1)-mCit was generated by overlap PCR using GGACCCCAATGCCAAGGTCGACGACAAGTGTACCTC-GTCAACC and GGTAGCACTT GTCGTGACCTTGGCATTGGGGTCTCATTCACC and cloned into mCit-N1 vector using the Nhe I and Acc 65I sites. mCherry-dynamitin was generated by cloning dynamitin in mCherry-C1 vector via the Hind III and Bsr GI sites. KIF13A(1-411) and KIF13A(1-411 Δ P) were PCR cloned into mCherry-FRB via Nhe I and Acc 65I restriction enzyme sites. FKBP-mCit-GTS

was made by replacing PX with GTS (Golgi-targeting sequence) in FKBP-mCit-PX (15). KIF13A(NC-CC1)-mCit, KIF13A(NC-CC1)-mCer, KIF13A(NC- Δ P-CC1)-mCit, and KIF13A(NC- Δ P-CC1)-mCer were cloned into pBiEx vector using the Kpn I and Sal I sites. Rab22A^{WT}, Rab22A^{Q64L}, and Rab22A^{S19N} were PCR cloned into pBiEx vector using the Age I and Not I sites. mCherry-syntaxin-13 was generated from GFP-syntaxin-13 by cloning into mCherry-C1. EEA1-mCherry and GFP-Rab35A were a gift from S. Arumugam (Monash University, Australia).

Cell culture, transfection, and epifluorescence

HeLa [cervical cancer cells, American Type Culture Collection (ATCC)] and COS-7 (monkey kidney fibroblast, ATCC) cells were maintained in Dulbecco's modified Eagle's medium (DMEM) with 10% fetal bovine serum (FBS; Invitrogen, India) and 2 mM L-glutamine at 37°C, 5% CO₂. CAD, a variant of a central nervous system catecholaminergic cell line, was maintained in F12/DMEM with 10% FBS and 2 mM L-glutamine at 37°C, 5% CO₂. HeLa cell line stably expressing GFP- α -tubulin was provided by D. Bhatia (Indian Institute of Technology Gandhinagar, India). For microscopy studies of fixed samples, cells were seeded at 1×10^5 cell density in six-well plates on acid-washed coverslips. Twenty-four hours after seeding, transfection was performed using Lipofectamine 3000 (Invitrogen) according to the manufacturer's protocol. Approximately 12 hours after transfection, samples were fixed in 4% (v/v) paraformaldehyde for 10 min, followed by incubation in 50 mM ammonium chloride for 5 min. The coverslips were mounted on glass slides using Pro-Long anti-fade mounting reagent (Thermo Fisher Scientific, India) and processed for image acquisition the next day. Images were obtained on an inverted epifluorescence and confocal microscope Nikon Eclipse Ti2-E, equipped with oil immersion 60 \times 1.49 numerical aperture (NA) objective and an Andor iXon Ultra 897 electron-multiplying charge-coupled device (EMCCD) camera.

For the RE tubulation analysis, three different parameters were manually quantified: (i) efficiency (percent transfected cells displaying RE tubulation), (ii) density (number of RE tubules per cell), and (iii) length (average length of RE tubules). RE tubulation efficiency was quantified into the following categories: (i) tubular REs, (ii) both tubular and vesicular REs, (iii) diffuse (no REs), and (iv) vesicular REs. Please refer to Fig. 1D for the depiction of these categories. Note that only cells containing more than two tubules, with length >5 μ m, were taken into account.

Live-cell imaging

For live-cell studies, HeLa cells were grown in glass-bottom dishes at 1×10^5 cell density, and transfection was performed as mentioned above. Live-cell imaging was performed 12 hours after transfection in FluoroBrite DMEM (Gibco) using TIRF microscopy: Nikon Eclipse Ti2-E, motorized automated, equipped with Perfect Focus System, oil immersion 60 \times , 1.49 NA objective, CO₂ chamber, Andor iXon Ultra 897 EMCCD camera, and NIS-Elements Advanced Research image acquisition software.

Nocodazole and ciliobrevin treatment

HeLa cells were cultured in 35-mm glass-bottom dishes and transfected with KIF13A-mCit or KIF13A(Δ P)-mCit, as mentioned previously. Cells were treated with 100 μ M ciliobrevin D (an inhibitor of the dynein ATPase activity) or 10 μ M nocodazole (for MT depolymerization) for 30 min, and movies were recorded using TIRF microscopy.

Transferrin recycling

HeLa cells were seeded on coverslips and transfected with KIF13A-mCit or KIF13A(Δ P)-mCit, as mentioned above. Twelve hours after transfection, cells were serum starved for 30 min at 37°C. Transferrin–Alexa Fluor 548 (20 μ g/ml) was internalized for 20 min in complete medium at 37°C. The cells were then washed with ice-cold phosphate-buffered saline (PBS) and chased with complete medium for 30 min at 37°C. Last, the slides were fixed as mentioned above and imaged with TIRF microscopy. CTFC [corrected total cell fluorescence = integrated density – (area of selected cell \times mean fluorescence of background readings)] analysis for recycling was measured using ImageJ (nih.gov).

Golgi scattering assay

To target KIF13A motors to the Golgi complex, we used chemically inducible FKBP/FRB heterodimerization system. First, we labeled the Golgi complex with Golgi-targeting sequence from HsGMAP210 fused to mCit and FKBP, a binding partner of FRB in the presence of rapamycin (GMAP210-mCit-FKBP). We tagged the C-terminal region of WT KIF13A(1-411) or KIF13A(1-411 Δ P) motors with mCherry-FRB (FKBP12-rapamycin binding domain). HeLa, COS-7, and CAD cells were seeded on glass-bottom dishes and cotransfected as mentioned above with FBKP-mCit-GTS and KIF13A(1-411)-mCherry-FRB or KIF13A(1-411 Δ P)-mCherry-FRB. Twelve hours after transfection, cells were treated with 1 μ M rapalog, an analog of rapamycin, to induce heterodimerization. Images were recorded at 0 and 30 min after treatment using TIRF microscopy. CAD cells were sensitive to continuous imaging (retract neurites and change their morphology); therefore, we performed time-lapse imaging to capture the dynamics of Golgi dispersion. Quantification of Golgi scattering was classified into the following categories based on their distribution inside the cell after adding rapalog: (i) tight (no dispersion, intact Golgi), (ii) perinuclear (slight dispersion), (iii) partial (moderate dispersion, mostly distributed throughout cytoplasm), and (iv) complete scattering (dispersed Golgi fragments accumulated at the cell periphery). Please refer to Fig. 2I for the schematic of these categories. Values were plotted as percentage of total transfected cells.

TIRF single-molecule motility assay

Single-molecule motility assays were performed using lysates of KIF13A motors overexpressed in COS-7. Cell lysates were prepared as described previously in (15). Tubulin purified from goat brains was used for MT polymerization in BRB80 [80 mM Pipes/KOH (pH 6.8), 1 mM MgCl₂, 1 mM EGTA] with 1 mM GTP, 37°C, 30 min. Polymerized MTs were stabilized by 1 μ M taxol and further diluted in P12 buffer [12 mM Pipes/KOH (pH 6.8), 1 mM MgCl₂, 1 mM EGTA]. MTs were passed into a flow chamber, which was assembled using double-sided tape between glass slide and a coverslip. After a 5-min incubation of MTs, blocking buffer [bovine serum albumin (BSA; 10 mg/ml) in P12] was added and incubated for 20 min. Last, motility mix containing the motor was infused into the flow chamber. Motility mix consisted of 0.1 to 5.0 μ l of COS-7 lysate, with or without bacterially purified dark Rab22A, 15 μ l of P12, 2 mM ATP, 1 mM dithiothreitol (DTT), 1 mM MgCl₂, glucose oxidase (0.2 mg/ml), catalase (0.08 mg/ml), and 10 μ M glucose. The flow chamber was sealed using melted wax and immediately imaged.

All imaging was performed at room temperature using a TIRF microscope (Nikon Ti2-E, motorized automated) equipped with oil immersion 100 \times 1.49 NA objective and Andor iXon Ultra 897 EMCCD camera. Images were recorded using 488-nm laser at 100-ms

exposure with no delay. Fluorescently labeled individual motors moving along the MT were tracked manually frame by frame to analyze single-molecule motility events using custom-written plugin for ImageJ (nih.gov) (15). Number of events for each sample was plotted for velocity and run length as a histogram and fit to a Gaussian distribution. Intermittent pauses and retraction were not considered while measuring velocity and run length.

Sf9 protein purification and bimolecular FRET assay

Sf9 culture, maintained in Sf900-II media (Gibco) at 28°C, 150 revolutions per minute, was transiently transfected with pBiEx constructs using Escort IV transfection reagent. Cells were harvested 72 hours after transfection and lysed in 0.5% IGEPAL, 4 mM MgCl₂, 200 mM NaCl, 7% sucrose, 20 mM Hepes, 5 mM DTT, aprotinin (5 μ g/ml), leupeptin (5 μ g/ml), and henylmethylsulfonyl fluoride (PMSF; 5 μ g/ml), pH 7.5. For purification, lysate was centrifuged [200,000 RCF (relative centrifugal force), 4°C, 30 min], and supernatant was incubated with anti-FLAG M2 affinity resin for 2 hours at 4°C, followed by three washes in 20 mM Hepes buffer containing 2 mM MgCl₂, 300 mM KCl, 2 mM DTT, aprotinin (5 μ g/ml), leupeptin (5 μ g/ml), and PMSF (5 μ g/ml), pH 7.5. Protein was finally eluted using FLAG peptide (100 μ g/ml).

Bimolecular FRET was performed in BRB80 buffer with BSA (0.1 mg/ml) using 15 nM mCer and 30 nM mCit sensors, in the absence or presence of 50 nM purified Rab22A. FRET sensors were purified from Sf9 cells, as described above. Spectra were recorded by excitation at 430 nm (8-nm bandpass) and emission at 450 to 600 nm (4-nm bandpass, 1-nm intervals) using a FluoroMax-4 spectrofluorometer (Horiba Scientific, USA). Spectra for mCit were subtracted from each sample to account for cross-excitation. Last, FRET ratio was calculated using intensity value at 525 and 475 nm.

Bacterial protein purification and biochemical assays

For His- and glutathione S-transferase (GST)-tagged protein purification, appropriate constructs were transformed into *Escherichia coli* BL21 pLys or BL21(DE3)pLysS and induced with 0.5 mM isopropyl β -D-1-thiogalactopyranoside at 25°C for 10 hours. Cells were harvested, followed by lysis with B-PER reagent (Thermo Fisher Scientific) containing 1 \times protease inhibitor cocktail, and purification was performed as per the manufacturer's instructions. The purified protein fractions were stored in 15% glycerol at –80°C in small aliquots.

Pull-down assays

For His pull-down, purified Rab proteins (5 μ g) were incubated with 15 μ l of preblocked Ni-NTA beads for 1 hour at 4°C in 50 mM Hepes buffer (pH 7.2) containing 150 mM NaCl and 2.5 mM EGTA. Beads were washed in PBS buffer containing 5 mM EDTA, 50 mM NaCl, and 0.15 mM PMSF. For binding assay, beads were incubated with increasing amounts of GST-tagged KIF13A NC-CC1 or NC- Δ P-CC1 (5 to 40 μ M) at 25°C for 20 min. Final washes of the beads were performed with 50 mM Hepes buffer (pH 7.2) containing 150 mM NaCl, 1 mM MgCl₂, and 0.2% Triton X-100. The beads were resuspended in 5 \times Laemmli buffer, subjected to 15% SDS–polyacrylamide gel electrophoresis (PAGE) gel electrophoresis. Immunoblotting was performed using anti-His or anti-GST monoclonal primary antibody (Invitrogen) and anti-mouse secondary antibody conjugated to peroxidase. Immunoblots were acquired using ChemiDoc MP Imaging System (Bio-Rad, USA).

For GST pull-down experiments, preblocked GST beads were incubated with approximately 10 μ g of GST-tagged KIF13A domain

fragments in 50 mM Hepes buffer (pH 7.2) with 150 mM NaCl and 2.5 mM EGTA for 1 hour at 4°C. Beads were then washed in PBS buffer containing 5 mM EDTA, 50 mM NaCl, and 0.15 mM PMSF, followed by incubation with 5 µg of purified 6x-His tagged Rab proteins for 1 hour at 4°C. Last, the beads were washed with 50 mM Hepes buffer (pH 7.2) containing 150 mM NaCl, 1 mM MgCl₂, and 0.2% Triton X-100. The beads were resuspended in 5× Laemmli buffer, ran on 15% SDS-PAGE gel, and immunoblotted using mouse anti-His or anti-GST monoclonal primary antibody (Invitrogen) and anti-mouse secondary antibody conjugated to peroxidase. Immunoblots were acquired using ChemiDoc MP Imaging System (Bio-Rad, USA). All biochemical assays were performed at least for three times from independent preparations.

Statistical analyses

Statistical analysis was performed using GraphPad Prism (8.0). Student's *t* test was calculated to determine statistical significance. PCC (Pearson correlation coefficient) values for colocalization and length of RE tubules were measured using NIS-Elements Advanced Research image acquisition and analysis software. Only cells containing more than two tubules, with length >5 µm, were taken into account. For quantification of RE tubule density and length, individual Z-stacks were considered. All data presented in this manuscript are from at least three independent experiments, unless otherwise mentioned.

SUPPLEMENTARY MATERIALS

Supplementary material for this article is available at <http://advances.sciencemag.org/cgi/content/full/7/6/eabd2054/DC1>

REFERENCES AND NOTES

- J. R. Goldenring, Recycling endosomes. *Curr. Opin. Cell Biol.* **35**, 117–122 (2015).
- B. D. Grant, J. G. Donaldson, Pathways and mechanisms of endocytic recycling. *Nat. Rev. Mol. Cell Biol.* **10**, 597–608 (2009).
- X. Li, E. Sapp, A. Valencia, K. B. Kegel, Z. H. Qin, J. Alexander, N. Masso, P. Reeves, J. J. Ritch, S. Zeitlin, N. Aronin, M. DiFiglia, A function of huntingtin in guanine nucleotide exchange on Rab11. *Neuroreport* **19**, 1643–1647 (2008).
- A. M. Schreij, E. A. Fon, P. S. McPherson, Endocytic membrane trafficking and neurodegenerative disease. *Cell. Mol. Life Sci.* **73**, 1529–1545 (2016).
- K. Etoh, M. Fukuda, Rab10 regulates tubular endosome formation through KIF13A and KIF13B motors. *J. Cell Sci.* **132**, jcs226977 (2019).
- S. Shakya, P. Sharma, A. M. Bhatt, R. A. Jani, C. Delevoye, S. R. Gangi Setty, Rab22A recruits BLOC-1 and BLOC-2 to promote the biogenesis of recycling endosomes. *EMBO Rep.* **19**, (2018).
- J. Rahajeng, S. S. Giridharan, B. Cai, N. Naslavsky, S. Caplan, MICAL-L1 is a tubular endosomal membrane hub that connects Rab35 and Arf6 with Rab8a. *Traffic* **13**, 82–93 (2012).
- E. S. Ward, C. Martinez, C. Vaccaro, J. Zhou, Q. Tang, R. J. Ober, From sorting endosomes to exocytosis: Association of Rab4 and Rab11 GTPases with the Fc receptor, FcRn, during recycling. *Mol. Biol. Cell* **16**, 2028–2038 (2005).
- R. Weigert, A. C. Yeung, J. Li, J. G. Donaldson, Rab22a regulates the recycling of membrane proteins internalized independently of clathrin. *Mol. Biol. Cell* **15**, 3758–3770 (2004).
- S. Takahashi, K. Kubo, S. Waguri, A. Yabashi, H. W. Shin, Y. Katoh, K. Nakayama, Rab11 regulates exocytosis of recycling vesicles at the plasma membrane. *J. Cell Sci.* **125**, 4049–4057 (2012).
- G. P. Solis, N. Hülsbusch, Y. Radon, V. L. Katanaev, H. Plattner, C. A. O. Stuermer, Reggins/fotillins interact with Rab11a and SNX4 at the tubulovesicular recycling compartment and function in transferrin receptor and E-cadherin trafficking. *Mol. Biol. Cell* **24**, 2689–2702 (2013).
- M. Sharma, S. S. Giridharan, J. Rahajeng, N. Naslavsky, S. Caplan, MICAL-L1 links EHD1 to tubular recycling endosomes and regulates receptor recycling. *Mol. Biol. Cell* **20**, 5181–5194 (2009).
- R. D. Vale, R. J. Fletterick, The design plan of kinesin motors. *Annu. Rev. Cell Dev. Biol.* **13**, 745–777 (1997).
- K. J. Verhey, N. Kaul, V. Soppina, Kinesin assembly and movement in cells. *Annu. Rev. Biophys.* **40**, 267–288 (2011).
- V. Soppina, S. R. Norris, A. S. Dizaji, M. Kortus, S. Veatch, M. Peckham, K. J. Verhey, Dimerization of mammalian kinesin-3 motors results in superprocessive motion. *Proc. Natl. Acad. Sci. U.S.A.* **111**, 5562–5567 (2014).
- V. Soppina, A. K. Rai, A. J. Ramaiya, P. Barak, R. Mallik, Tug-of-war between dissimilar teams of microtubule motors regulates transport and fission of endosomes. *Proc. Natl. Acad. Sci. U.S.A.* **106**, 19381–19386 (2009).
- S. M. Block, Kinesin motor mechanics: Binding, stepping, tracking, gating, and limping. *Biophys. J.* **92**, 2986–2995 (2007).
- N. Siddiqui, A. Straube, Intracellular cargo transport by kinesin-3 motors. *Biochemistry* **82**, 803–815 (2017).
- K. I. Schimert, B. G. Budaitis, D. N. Reinemann, M. J. Lang, K. J. Verhey, Intracellular cargo transport by single-headed kinesin motors. *Proc. Natl. Acad. Sci. U.S.A.* **116**, 6152–6161 (2019).
- R. Mallik, B. C. Carter, S. A. Lex, S. J. King, S. P. Gross, Cytoplasmic dynein functions as a gear in response to load. *Nature* **427**, 649–652 (2004).
- A. Rai, D. Pathak, S. Thakur, S. Singh, A. K. Dubey, R. Mallik, Dynein clusters into lipid microdomains on phagosomes to drive rapid transport toward lysosomes. *Cell* **164**, 722–734 (2016).
- A. K. Rai, A. Rai, A. J. Ramaiya, R. Jha, R. Mallik, Molecular adaptations allow dynein to generate large collective forces inside cells. *Cell* **152**, 172–182 (2013).
- E. N. Anderson, J. A. I. White, S. Gunawardena, Axonal transport and neurodegenerative disease: Vesicle-motor complex formation and their regulation. *Degener. Neurol. Neuromuscul. Dis.* **4**, 29–47 (2013).
- M. A. Franker, C. C. Hoogenraad, Microtubule-based transport – basic mechanisms, traffic rules and role in neurological pathogenesis. *J. Cell Sci.* **126**, 2319–2329 (2013).
- N. Hirokawa, S. Niwa, Y. Tanaka, Molecular motors in neurons: Transport mechanisms and roles in brain function, development, and disease. *Neuron* **68**, 610–638 (2010).
- C. Delevoye, S. Miserey-Lenkei, G. Montagnac, F. Gilles-Marsens, P. Paul-Gilloteaux, F. Giordano, F. Waharte, M. S. Marks, B. Goud, G. Raposo, Recycling endosome tubule morphogenesis from sorting endosomes requires the kinesin motor KIF13A. *Cell Rep.* **6**, 445–454 (2014).
- K. T. O'Neil, W. F. DeGrado, A thermodynamic scale for the helix-forming tendencies of the commonly occurring amino acids. *Science* **250**, 646–651 (1990).
- L. Piel, G. Nemethy, H. A. Scheraga, Proline-induced constraints in alpha-helices. *Biopolymers* **26**, 1587–1600 (1987).
- H. R. Wilman, J. Shi, C. M. Deane, Helix kinks are equally prevalent in soluble and membrane proteins. *Proteins* **82**, 1960–1970 (2014).
- S. Yohannan, S. Faham, D. Yang, J. P. Whitelegge, J. U. Bowie, The evolution of transmembrane helix kinks and the structural diversity of G protein-coupled receptors. *Proc. Natl. Acad. Sci. U.S.A.* **101**, 959–963 (2004).
- J. Ren, L. Huo, W. Wang, Y. Zhang, W. Li, J. Lou, T. Xu, W. Feng, Structural correlation of the neck coil with the coiled-coil (CC1)-Forkhead-associated (FHA) tandem for active kinesin-3 KIF13A. *J. Biol. Chem.* **291**, 3581–3594 (2016).
- J. Ren, S. Wang, H. Chen, W. Wang, L. Huo, W. Feng, Coiled-coil 1-mediated fastening of the neck and motor domains for kinesin-3 autoinhibition. *Proc. Natl. Acad. Sci. U.S.A.* **115**, E11933–E11942 (2018).
- S. Hoepfner, F. Severin, A. Cabezas, B. Habermann, A. Runge, D. Gillyooly, H. Stenmark, M. Zerial, Modulation of receptor recycling and degradation by the endosomal kinesin KIF16B. *Cell* **121**, 437–450 (2005).
- R. Prekeris, J. Klumperman, Y. A. Chen, R. H. Scheller, Syntaxin 13 mediates cycling of plasma membrane proteins via tubulovesicular recycling endosomes. *J. Cell Biol.* **143**, 957–971 (1998).
- A. G. Hendricks, E. Perlson, J. L. Ross, H. W. Schroeder III, M. Tokito, E. L. F. Holzbaur, Motor coordination via a tug-of-war mechanism drives bidirectional vesicle transport. *Curr. Biol.* **20**, 697–702 (2010).
- X. Li, N. Rydzewski, A. Hider, X. Zhang, J. Yang, W. Wang, Q. Gao, X. Cheng, H. Xu, A molecular mechanism to regulate lysosome motility for lysosome positioning and tubulation. *Nat. Cell Biol.* **18**, 404–417 (2016).
- V. Marchesin, A. Castro-Castro, C. Lodillinsky, A. Castagnino, J. Cyra, H. Bonsang-Kitzis, L. Fuhrmann, M. Irondelle, E. Infante, G. Montagnac, F. Rey, A. Vincent-Salomon, P. Chavrier, ARF6-JIP3/4 regulate endosomal tubules for MT1-MMP exocytosis in cancer invasion. *J. Cell Biol.* **211**, 339–358 (2015).
- A. Mrakovic, J. G. Kay, W. Furuya, J. H. Brumel, R. J. Botelho, Rab7 and Arl8 GTPases are necessary for lysosome tubulation in macrophages. *Traffic* **13**, 1667–1679 (2012).
- J. K. Burkhardt, C. J. Echeverri, T. Nilsson, R. B. Vallee, Overexpression of the dynamitin (p50) subunit of the dynactin complex disrupts dynein-dependent maintenance of membrane organelle distribution. *J. Cell Biol.* **139**, 469–484 (1997).
- A. J. Firestone, J. S. Weinger, M. Maldonado, K. Barlan, L. D. Langston, M. O'Donnell, V. I. Gelfand, T. M. Kapoor, J. K. Chen, Small-molecule inhibitors of the AAA+ ATPase motor cytoplasmic dynein. *Nature* **484**, 125–129 (2012).
- M. F. Engelke, M. Winding, Y. Yue, S. Shastry, F. Teloni, S. Reddy, T. L. Blasius, P. Soppina, W. O. Hancock, V. I. Gelfand, K. J. Verhey, Engineered kinesin motor proteins amenable to small-molecule inhibition. *Nat. Commun.* **7**, 11159 (2016).

42. M. M. Nguyen, C. J. McCracken, E. S. Milner, D. J. Goetschius, A. T. Weiner, M. K. Long, N. L. Michael, S. Munro, M. M. Rolls, γ -Tubulin controls neuronal microtubule polarity independently of Golgi outposts. *Mol. Biol. Cell* **25**, 2039–2050 (2014).
43. Y. Chen, P. L. Chen, C. F. Chen, Z. D. Sharp, W. H. Lee, Thyroid hormone, T3-dependent phosphorylation and translocation of Trip230 from the Golgi complex to the nucleus. *Proc. Natl. Acad. Sci. U.S.A.* **96**, 4443–4448 (1999).
44. J. W. Hammond, D. Cai, T. L. Blasius, Z. Li, Y. Jiang, G. T. Jih, E. Meyhofer, K. J. Verhey, Mammalian Kinesin-3 motors are dimeric in vivo and move by processive motility upon release of autoinhibition. *PLoS Biol.* **7**, e72 (2009).
45. T. M. Huckaba, A. Gennerich, J. E. Wilhelm, A. H. Chishti, R. D. Vale, Kinesin-73 is a processive motor that localizes to Rab5-containing organelles. *J. Biol. Chem.* **286**, 7457–7467 (2011).
46. M. Tomishige, D. R. Klopfenstein, R. D. Vale, Conversion of Unc104/KIF1A kinesin into a processive motor after dimerization. *Science* **297**, 2263–2267 (2002).
47. A. Bielli, P.-O. Thörnqvist, A. G. Hendrick, R. Finn, K. Fitzgerald, M. W. McCaffrey, The small GTPase Rab4A interacts with the central region of cytoplasmic dynein light intermediate chain-1. *Biochem. Biophys. Res. Commun.* **281**, 1141–1153 (2001).
48. I. Grigoriev, D. Splinter, N. Keijzer, P. S. Wulf, J. Demmers, T. Ohtsuka, M. Modesti, I. V. Maly, F. Grosveld, C. C. Hoogenraad, A. Akhmanova, Rab6 regulates transport and targeting of exocytotic carriers. *Dev. Cell* **13**, 305–314 (2007).
49. C. P. Horgan, S. R. Hanscom, R. S. Jolly, C. E. Futter, M. W. McCaffrey, Rab11-FIP3 links the Rab11 GTPase and cytoplasmic dynein to mediate transport to the endosomal-recycling compartment. *J. Cell Sci.* **123**, 181–191 (2010).
50. I. Jordens, M. Fernandez-Borja, M. Marsman, S. Dusseljee, L. Janssen, J. Calafat, H. Janssen, R. Wubbolts, J. Neefjes, The Rab7 effector protein RILP controls lysosomal transport by inducing the recruitment of dynein-dynactin motors. *Curr. Biol.* **11**, 1680–1685 (2001).
51. E. Schonteich, G. M. Wilson, J. Burden, C. R. Hopkins, K. Anderson, J. R. Goldenring, R. Prekeris, The Rip11/Rab11-FIP5 and kinesin II complex regulates endocytic protein recycling. *J. Cell Sci.* **121**, 3824–3833 (2008).
52. B. Short, C. Preisinger, J. Schaletzky, R. Kopajtich, F. A. Barr, The Rab6 GTPase regulates recruitment of the dynactin complex to Golgi membranes. *Curr. Biol.* **12**, 1792–1795 (2002).
53. P. L. Lee, M. B. Ohlson, S. R. Pfeffer, Rab6 regulation of the kinesin family KIF1C motor domain contributes to Golgi tethering. *eLife* **4**, e06029 (2015).

Acknowledgments: V.S. thanks K. J. Verhey and R. Mallik for unconditional support throughout the study. V.S. also thanks P. Soppina, A. Rai, and P. Barak for their valuable input on the manuscript. **Funding:** V.S. acknowledges funding through DBT (grant nos. BT/PR15214/BRB/10/1449/2015 and BT/RLF/re-entry/45/2015) and DST-SERB (grant no. ECR/2016/000913). N.M.P., M.S.A.S., and D.J.S. acknowledge fellowship from IIT Gandhinagar. S.S. acknowledges funding from the NIH (1R35GM126940-02). S.R.G.S. acknowledges funding from India Alliance (500122/Z/09/Z), SERB (CRG/2019/000281), and DBT (NBACD-2019), and IISc graduate fellowship to P.S. **Author contributions:** N.M.P., M.S.A.S., A.R., S.S., and V.S. designed the research; N.M.P., M.S.A.S., R.K., D.J.S., and V.S. performed the experiments; N.M.P., M.S.A.S., D.J.S., M.R., A.R., and V.S. analyzed the data; and N.M.P., M.S.A.S., and V.S. wrote the paper with constant feedback and comments from other authors and lab members. **Competing interests:** The authors declare that they have no competing interests. **Data and materials availability:** All data needed to evaluate the conclusions in the paper are present in the paper and/or the Supplementary Materials. Additional data related to this paper may be requested from the authors.

Submitted 7 June 2020
Accepted 16 December 2020
Published 3 February 2021
10.1126/sciadv.abd2054

Citation: N. M. Patel, M. S. A. Siva, R. Kumari, D. J. Shewale, A. Rai, M. Ritt, P. Sharma, S. R. G. Setty, S. Sivaramakrishnan, V. Soppina, KIF13A motors are regulated by Rab22A to function as weak dimers inside the cell. *Sci. Adv.* **7**, eabd2054 (2021).

KIF13A motors are regulated by Rab22A to function as weak dimers inside the cell

Nishaben M. Patel, Meenakshi Sundaram Aravintha Siva, Ruchi Kumari, Dipeshwari J. Shewale, Ashim Rai, Michael Ritt, Perna Sharma, Subba Rao Gangi Setty, Sivaraj Sivaramakrishnan and Virupakshi Soppina

Sci Adv 7 (6), eabd2054.
DOI: 10.1126/sciadv.abd2054

ARTICLE TOOLS	http://advances.sciencemag.org/content/7/6/eabd2054
SUPPLEMENTARY MATERIALS	http://advances.sciencemag.org/content/suppl/2021/02/02/7.6.eabd2054.DC1
REFERENCES	This article cites 52 articles, 23 of which you can access for free http://advances.sciencemag.org/content/7/6/eabd2054#BIBL
PERMISSIONS	http://www.sciencemag.org/help/reprints-and-permissions

Use of this article is subject to the [Terms of Service](#)

Science Advances (ISSN 2375-2548) is published by the American Association for the Advancement of Science, 1200 New York Avenue NW, Washington, DC 20005. The title *Science Advances* is a registered trademark of AAAS.

Copyright © 2021 The Authors, some rights reserved; exclusive licensee American Association for the Advancement of Science. No claim to original U.S. Government Works. Distributed under a Creative Commons Attribution NonCommercial License 4.0 (CC BY-NC).